

Cite this: *Org. Chem. Res.* **2022**, Vol. 8, 48-56.

DOI: 10.22036/org.chem.2023.423424.1299

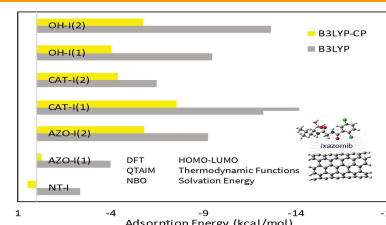
# Investigating the Adsorption Behavior of Organic-functionalized Carbon Nanotubes via Hydrogen Bonds for Delivery of Ixazomib Anticancer Drug

Seyedeh Fatemeh Sadat Mazloun Hosseini<sup>a</sup> , Mansoureh Zahedi-Tabrizi<sup>a,\*</sup> , Zainab Moosavi-Tekyeh<sup>b</sup> <sup>a</sup>Department of Physical Chemistry and Nanochemistry, Faculty of Chemistry, Alzahra University, P. O. Box: 1993893973, Tehran, Iran, E-mail: Zahedi@alzahra.ac.ir<sup>b</sup>Department of Chemistry, Shahrood University of Technology, P. O. Box: 3619995161, Shahrood, Iran

Received: November 2, 2023; Accepted: November 22, 2023

**Abstract:** Functionalization of (5,5) single-walled carbon nanotubes (SWNTs) with 1,3-dipolar cycloaddition of azomethine ylide, 4-catechol, and hydroxyl substituents was investigated for delivering ixazomib (IXA) at the B3LYP level of theory with 6-31G (d, p) basis set. The adsorption energies for two different functionalized NT/IXA configurations were calculated in the gas phase. The strength of intermolecular hydrogen bonds (IHBs) in the optimized structures was compared using the quantum theory of atoms in molecules (QTAIM). Catechol and OH-functionalized NT/IXA complexes indicate higher adsorption energies because of intermolecular hydrogen bonds (IHBs) in these drug delivery systems. A detailed study of the delocalization interactions in IHB bridges was performed by natural bond orbital (NBO) analysis. The long-range corrected hybrid density functional's effect on adsorption energies was evaluated for more stable configurations. Moreover, a comparison was made between the conceptual DFT descriptors of complexes by molecular orbital (MO) analysis. Analysis of thermodynamic parameters and solvation energies demonstrates the potential application of these organic-functionalized NTs, especially OH-functionalized NTs, as carriers for the IXA drug.

**Keywords:** Ixazomib, DFT, Hydroxyl functionalized CNT, Catechol, Azomethine ylide



## 1. Introduction

*Multiple myeloma* is a bone marrow-based cancer that causes malignant disorders in plasma cells. In this case, the cancer cells produce abnormal proteins instead of helpful antibodies.<sup>1</sup> Ixazomib (C<sub>14</sub>H<sub>19</sub>BCl<sub>2</sub>N<sub>2</sub>O<sub>4</sub>), N<sub>2</sub>-(2,5-dichlorobenzoyl)-N-[(1R)-1-(dihydroxyboryl)-3-methylbutyl] glycinamide (PubChem: 25183872), under the brand name Ninlaro, is a citrate ester of boric acid used with dexamethasone and lenalidomide to treat this cancer. When exposed to aqueous solutions (gastrointestinal tract or plasma), this drug is hydrolyzed and converted to the active form of boric acid.<sup>2</sup> The side effects of this drug include neutropenia, thrombocytopenia, rash, and fatigue.<sup>3</sup>

In conventional cancer treatment methods, including chemotherapy, drugs are distributed throughout the body and cause side effects.<sup>4</sup> One of the essential objectives in the pharmaceutical industry is the targeted and controlled delivery of drugs to the body to increase the drug's efficacy and reduce its side effects. The primary objective of designing and developing drug delivery systems is to achieve a system that has appropriate drug loading, optimal release properties with long half-lives, and low toxicity. Nanotechnology has enabled targeted drugs that control the time, place, and rate of drug release in the body. In this regard, polymeric micelles,<sup>5,6</sup> dendrimers,<sup>7</sup> liposomes,<sup>8</sup> and hydrogels<sup>9</sup> have been utilized as potential carriers of anticancer drugs. Therefore, numerous

studies have investigated the interactions between anticancer drugs and drug delivery systems based on these nanomaterials. For example, a system of catechol-bearing antioxidant micelles was introduced by Hasegawa et al.<sup>10</sup> to carry bortezomib (a drug similar to ixazomib) to treat cancer cells with chemotherapy. Additionally, a delivery system based on biodegradable micelles showed that this system is a targeted delivery of bortezomib, which leads to the accumulation of the drug in cancer cells and enhances the treatment efficacy.<sup>11</sup> In the following, designing nanodrug delivery systems based on biocompatible polymers such as glycine poly-L-lactic acid nanoparticles has been beneficial regarding safety and cytotoxicity effects.<sup>12</sup>

Carbon nanotubes<sup>13</sup> have also been used as carriers of anticancer drugs. The small diameter of these nanoparticles allows them to easily cross the cell membrane and biological barriers and enter the cell. Additionally, their high capacity to load drugs is the reason for introducing them as another potential candidate for carrying various drugs.<sup>14,15</sup> NTs can adsorb and store drugs with covalent, noncovalent, and hydrogen bonds on the surface of their sidewalls or inside their capsules.<sup>16</sup> The limitations of using NTs are due to their hydrophobicity, which can be eliminated by substituting them with various functional groups, mineral biomolecules, and polymers.<sup>17</sup> Considering the importance of drug delivery systems in reducing the side effects of direct absorption of

ixazomib (IXA), predicting an appropriate drug delivery system is particularly significant. Therefore, in this study, functionalized NTs (*f*-NTs) with 1,3-dipolar cycloaddition of azomethine ylides (AZO), 4-catechol (CAT), and hydroxyl (OH) substitutions were selected as drug delivery systems to reduce the toxicity of pure nanotubes. The main purpose of this investigation is to select the most appropriate drug delivery system by density functional theory (DFT) calculations. Moreover, long-range corrected hybrid density functionals have been considered to study dispersion corrections.

## 2. Details of the calculations

Due to the extensive use of (5,5) NTs and *f*-NTs in drug delivery systems,<sup>18</sup> we considered the interactions of IXA with pure (5,5) armchair single-walled NT and *f*-NTs with 1,3-dipolar cycloaddition of azomethine ylides (AZO-NT), 4-catechol (CAT-NT), and hydroxyl (OH-NT) substituents. A pristine (5,5) open-ended armchair NT (C<sub>100</sub>H<sub>20</sub>) was modeled<sup>19</sup> and optimized at the B3LYP/6-31G (d, p) level of theory. The optimized structure of NT with a length of 12.917 Å and a diameter of 7.489 Å was selected for modeling the *f*-NTs. For a better comparison of the adsorption behavior of *f*-NTs, only one catechol group (which consists of two syn-OH groups) was added to the surface of NT. Therefore, to correct the spin multiplicity in CAT-NT, one hydrogen atom was added to the end of the tube.

As in many bioapplications, hydroxyl groups at the end of NTs can be coupled with biomolecules;<sup>15</sup> in OH-NT modeling, the two hydroxyl groups were substituted on the NT sidewall, and ten hydroxyl groups were added at two ends of the NT. First, all of the *f*-NTs and functionalized nanotube-IXA (*f*-I) complexes were fully optimized by the DFT method at the B3LYP level, Becke three-parameter hybrid functional, which includes both local and nonlocal correlation terms provided by LYP expression<sup>20,21</sup> with a 6-31G (d, p) basis set by the Gaussian 09 package of a program.<sup>22</sup> Then, more stable complexes were fully optimized with the same basis set at the ωB97XD functional. ωB97XD is a long-range corrected functional from Chai and Head-Gordon,<sup>23</sup> which uses Grimm's D2 dispersion model. The adsorption energy (E<sub>ads</sub>), the deformation energy of IXA or *f*-NT (E<sub>def-I</sub> (or *f*-NT)), and the interaction energy (E<sub>int</sub>) were obtained using the following equations:<sup>24</sup>

$$E_{\text{ads}} = E_{\text{complex}} - (E_{f\text{-NT}} + E_{\text{IXA}}) \quad (1)$$

$$E_{\text{def-IXA(or } f\text{-NT)}} = E_{\text{IXA(or } f\text{-NT) in complex}} - E_{\text{IXA(or } f\text{-NT)}} \quad (2)$$

$$E_{\text{int}} = E_{\text{ads}} - (E_{\text{def-}f\text{-NT}} + E_{\text{def-IXA}}) \quad (3)$$

where E<sub>complex</sub>, E<sub>*f*-NT</sub>, and E<sub>IXA</sub> are the total electronic energy of the complex containing the nanotube and drug, the

nanotube (pure and functional), and the drug, respectively. The adsorption energy (E<sub>ads</sub>) is composed of two parts: deformation energy (E<sub>def</sub>), and interaction energy (E<sub>int</sub>). E<sub>def</sub> is calculated as the difference between the total electronic energy of the molecule in the complex and its fully optimized structure.

Boys and Bernardi's counterpoise approach has been used to calculate the basis set superposition error (BSSE) to correct the adsorption energies.<sup>25</sup> Topological electron density analysis was performed at B3LYP computational level for all the optimized structures by the quantum theory of atoms in molecules (QTAIM) and the AIM2000 program.<sup>26,27</sup> Additionally, natural bond orbital (NBO) analysis was performed at the same level of theory using the NBO 3.1 module under the Gaussian program package.<sup>28-31</sup>

The energy difference between the HOMO (highest occupied molecular orbital) and LUMO (lowest unoccupied molecular orbital) is defined as follows:

$$E_g = E_{\text{LUMO}} - E_{\text{HOMO}} \quad (4)$$

For the N-electron systems, the chemical hardness (η)<sup>32,33</sup> was calculated as

$$\eta = \frac{E_g}{2} \quad (5)$$

HOMO-LUMO diagrams were plotted by the GaussView program<sup>34</sup> at B3LYP computational level and the GaussSum<sup>35</sup> program was employed to obtain density of state (DOS) plots. Thermodynamic parameters, including the standard Gibbs free energy change, the standard enthalpy change, and the standard entropy change of the adsorption process at 298.15 K and 1.0 atm pressure, were calculated using the following equations:

$$\Delta_{\text{ads}}H^\circ = [H_{\text{complex}}^\circ] - ([H_{f\text{-NT}}^\circ] + [H_{\text{IXA}}^\circ]) \quad (6)$$

$$\Delta_{\text{ads}}G^\circ = [G_{\text{complex}}^\circ] - ([G_{f\text{-NT}}^\circ] + [G_{\text{IXA}}^\circ]) \quad (7)$$

where H<sup>°</sup> is the sum of the electronic and thermal enthalpy (a shortcut in frequency output), and G<sup>°</sup> is the sum of the electronic and thermal free energy. The standard entropy change of adsorption could be obtained by the thermodynamic relation of Δ<sub>ads</sub>H<sup>°</sup> and Δ<sub>ads</sub>G<sup>°</sup> or by the difference of the sum of the total standard entropy of the reactant and products. The solvation energy (SE) was defined as

$$SE = G_{\text{liquid phase}}^\circ - G_{\text{gas phase}}^\circ \quad (8)$$

The frequency calculations in the water solvent were performed, employing the self-consistent reaction field (SCRf) and Tomasi's polarizable continuum model (PCM).<sup>36</sup>

The water solvent is selected because of the importance of aqueous solutions in studying biological processes.

### 3. Results and Discussion

To achieve the most stable model for each *f*-I complex, two different configurations were modeled by rotating the drug on the surface of each *f*-NT. In the considered models, the IXA molecule distance from NTs was scanned to the outer surface of the NTs, allowing for minimum steric effects and appropriate sites for IHB formation. The optimized structures of IXA and *f*-I complexes computed at B3LYP/6-31G (d, p) in the gas phase are shown in Figures 1 and 2, respectively. In the IXA orientation on the pure NT surface,  $\pi$ - $\pi$  stacking or pi-pi interactions<sup>37</sup> between the para-dichlorobenzene ring of IXA and NT aromatic hexagonal rings have been determinative. All the optimized structures of *f*-I complexes at B3LYP/6-31G (d, p) are presented in Figure 3.

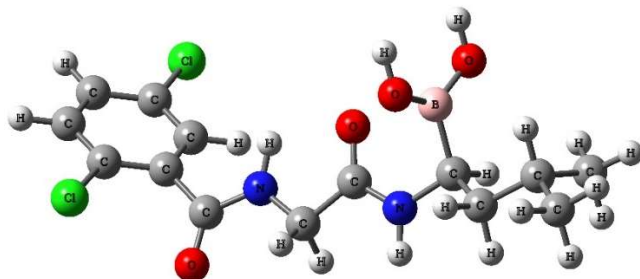


**Figure 1.** Optimized structure of IXA computed at B3LYP/6-31G (d, p) in the gas phase.

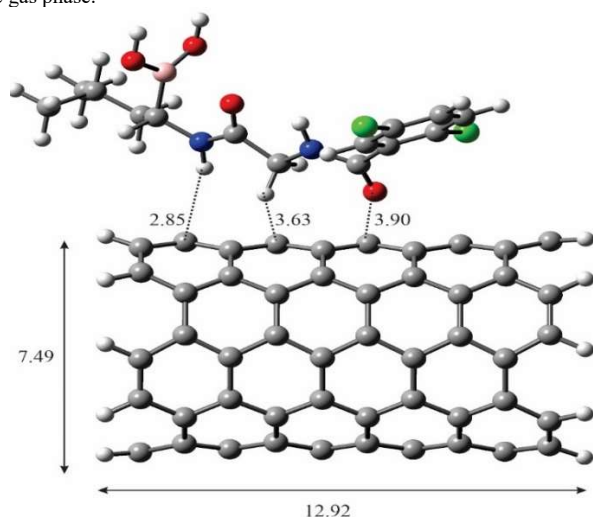


**Figure 2.** Optimized structure of the NT-I complex computed at B3LYP/6-31G (d, p) in the gas phase. Numbers are in Å.

#### Molecular geometry and adsorption energy

A detailed analysis of the optimized structure of NT-I in Figure 2 shows that the length and diameter of pure NT are almost identical (the mean variation is approximately 0.004 Å) before and after drug adsorption. The adsorption energies of IXA on the surface of *f*-NTs are listed in Table 1. In a comprehensive interpretation, this table shows that NT

functionalization increases the adsorption energy. According to the third column of Table 1, the BSSE-counterpoise corrected (CP corr.) adsorption energies of *f*-I complexes change from -0.28 to -7.59 kcal/mol in the gas phase.

**Table 1.** Adsorption energies in the gas phase ( $E_{ads}$ ), the BSSE-counterpoise corrected (CP corr.) adsorption energy, deformation energy of NT ( $E_{def-NT}$ ), deformation energy of ixazomib ( $E_{def-IXA}$ ), interaction energy ( $E_{int}$ ), and CP corr.  $E_{int}$ , (all in kcal/mol), calculated at B3LYP/6-31G (d, p) level of theory

Complex	$E_{ads}$	$E_{ads}$ (CP corr.)	$E_{def-NT}$	$E_{def-IXA}$	$E_{int}$	$E_{int}$ (CP corr.)
NT-I	-2.37	0.47	0.76	0.13	-3.26	-0.43
AZO-I(1)	-4.02	-0.28	0.06	0.28	-4.35	-0.61
AZO-I(2)	-9.25	-5.85	0.10	0.65	-10.00	-6.59
CAT-I(1)	-14.18	-7.59	0.73	1.39	-16.31	-9.72
CAT-I(2)	-6.50	-4.43	0.15	0.17	-6.81	-4.74
OH-I(1)	-9.51	-4.10	0.26	1.18	-10.95	-5.54
OH-I(2)	-12.68	-5.79	1.59	0.48	-14.75	-7.86

The trend of the calculated adsorption energies did not change after the BSSE correction. The low adsorption energies (less negative) imply the physical adsorption of the IXA molecule on the *f*-NT surfaces. In addition, the comparison of adsorption energies shows that CAT-I(1) and OH-I(2) complexes have the highest adsorption energies (more negative). As a consequence, these two complexes are the most stable configurations in terms of adsorption energy. Notably, the nanotube interacts with the carbonyl group of IXA in these two structures. In CAT-I(1), the carbonyl group between the N atoms of the IXA molecule interacts with the OH groups of catechol in CAT-NT. However, in OH-I(2), the carbonyl group near the para-dichlorobenzene ring of the IXA molecule interacts with two OH groups of the NT sidewall (Figure 3).

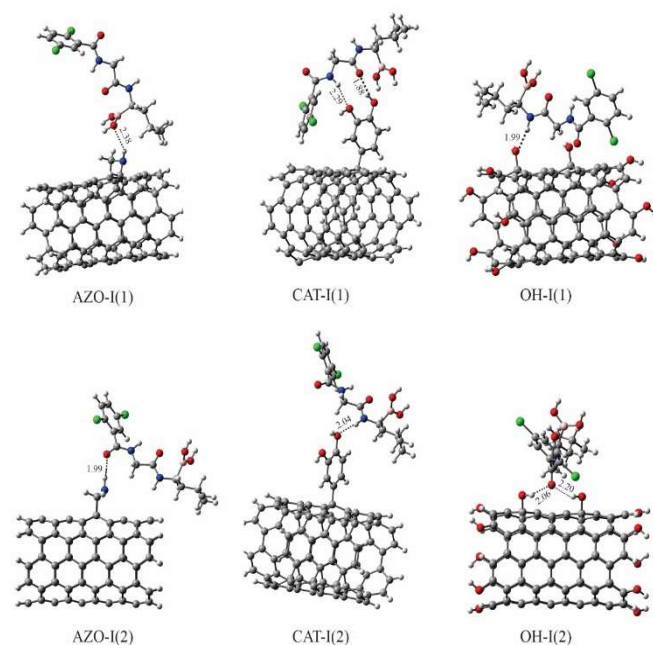


**Figure 3.** Optimized structures of AZO-I(1), AZO-I(2), CAT-I(1), CAT-I(2), OH-I(1), and OH-I(2) complexes computed at B3LYP/6-31G (d, p) in the gas phase. All numbers are in Å.



A comparison between optimized structural parameters of IXA, including bond length, bond angles, and dihedral angles, with the same geometrical parameters of IXA in complex showed that the structural parameters of the drug have little variation before and after loading on the surface of NTs. The low values of the total electronic energy difference between IXA in the complex and the optimized structure of IXA or  $E_{def-IXA}$  (see Table 1) confirm the conservation of the IXA structure in the complex and its physical adsorption. Therefore, the drug's therapeutic properties will be preserved after adsorption on NTs, which could be vital in selecting drug delivery systems.

### QTAIM analysis

Bader et al.<sup>38</sup> proposed a method known as the QTAIM to study the sharing of electrons between atoms in a molecule. According to this theory, the topology of the electron density ( $\rho_{BCP}$ ) and its Laplacian ( $\nabla^2\rho_{BCP}$ ) at the bond critical points (BCPs) describe the structure of molecules. These parameters have been calculated in many HB studies<sup>39-42</sup> and NT adsorption-desorption processes.<sup>43</sup>

To understand the reason for the increasing adsorption energies in CAT-I(1) and OH-I(2), a complete QTAIM analysis was performed, which provided exciting insight into the IHBs. A set of topological parameters of the IHB has been collected in Table 2. As seen in this table, the electron density at the bond critical points ( $\rho(r)$ ) for all complexes is positive and within the range 0.005-0.025 a.u., which indicates closed-shell interactions such as hydrogen bonding. Moreover,  $\nabla^2\rho$  at BCPs ( $\nabla^2\rho(r)$ ) is positive for all of the complexes, which points to the weak hydrogen bonds or electrostatic nature of hydrogen bonds. The hydrogen bond energy was estimated by the  $E_{HB} = 0.5 V(r)$  formula.<sup>44</sup>

The molecular graph of CAT-I(1) calculated at B3LYP/6-31G(d, p) in the gas phase is shown in Figure 4. Three considerable BCPs between IXA and CAT-NT in the CAT-I(1) complex were found. These BCPs have formed one stronger IHB, including O-H\*...O=C (the \* symbol represents the NT) with 6.12 kcal/mol (the fourth row of Table 2), which has been classified as weak hydrogen bonds.<sup>45,46</sup> The H\*...O distance in this hydrogen bond is 1.885 Å. In this hydrogen bond, the hydroxyl group of catechol is a proton donor (see Figure 3), and the carbonyl group between the N atoms in ixazomib is a proton acceptor. According to the QTAIM results, another BCP was found between the oxygen atom of the catechol group as a proton acceptor and the H-O-B group of IXA as a proton donor (4.83 kcal/mol). Furthermore, the weakest hydrogen bond between the NH groups of IXA as a proton donor and the oxygen atom of the OH group in catechol as a proton acceptor was found. According to the QTAIM results, this hydrogen bond is weak (2.79 kcal/mol). These results can explain the highest adsorption energy in the CAT-I(1) complex.

Considering the adsorption energies in Table 1, significant IHBs were expected in the OH-I(2) complex. The carbonyl

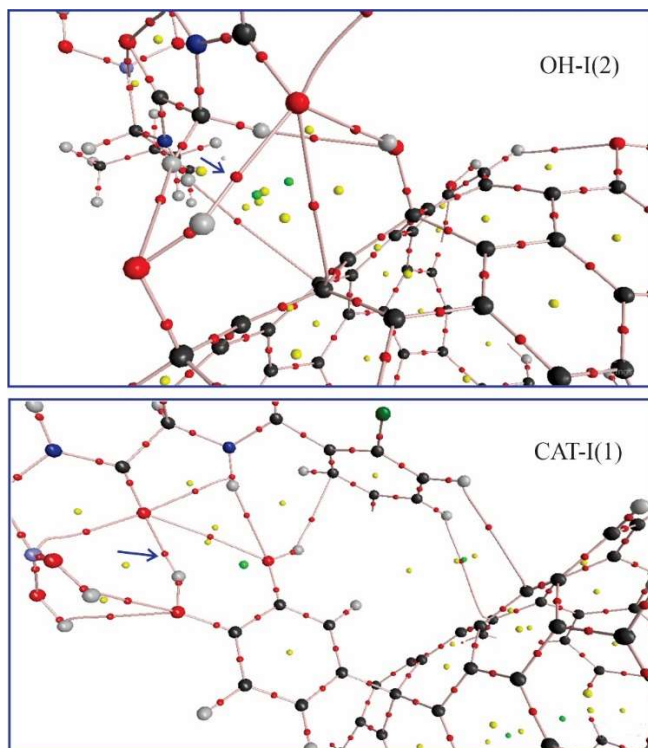


**Figure 4.** The molecular graph of OH-I(2) and CAT-I(1) calculated at B3LYP/6-31G(d, p) in the gas phase. The small red and yellow spheres represent the BCPs and RCPs, respectively. The blue arrow denotes the strongest IHB.

group near the para-dichlorobenzene ring of IXA formed two BCPs with two OH groups on the sidewall of OH-NT. As expected, the carbonyl group could be a proton acceptor from two hydroxyl groups. The sum of these hydrogen bond energies was obtained at approximately 7.94 kcal/mol. Moreover, two weak hydrogen bonds were found between the hydroxyl group of OH-NT as a proton acceptor and the CH groups of IXA as a proton donor. In the first study of IHBs using QTAIM data, we did not consider very weak IHBs between the C-H groups of IXA (as a proton donor) and the OH groups of OH-NT. After examining the charge transfers between IXA and OH-NT in the next section of computations, we realized that the charge transfer in this IHB cannot be ignored. In general, it can be concluded that IHBs have made an essential contribution to the adsorption energies of CAT-I(1) and OH-I(2) complexes.

It is worth mentioning that the absolute values of NT-I and AZO-I interaction energies ( $E_{int}$ ) before CP correction were obtained more than the HB energy. However, after CP correction ( $E_{int, CP Corr.}$ ), these values were less than the HB energy (see Table 1 and Table 2). The inconsistency of this outcome can be explained by considering that the HB energy values calculated by QTAIM analysis are not exact energies and only indicate the trend of HB strength. For a deeper understanding of the interactions in the *f*-I complexes in the next section, we performed NBO analysis, providing better insight into the charge transfers and electrostatic interactions.

**Table 2.** Hydrogen bond (HB) length (Å), topological parameters (all in a. u.), and HB energy formation (in kcal/mol) calculated at B3LYP/6-31G (d, p). The \* symbol represents the NT atom

Complex	HB Atoms	HB length	$\rho(r) \times 10^{-4}$	$\nabla^2\rho(r) \times 10^{-4}$	$V(r) \times 10^{-4}$	$E_{HB}$
NT-I	C-C*...H-N	2.852	55	160	-24	0.75
AZO-I(1)	N-H*...O-B	2.380	115	364	-83	2.60
AZO-I(2)	N-H*...O=C	1.994	232	664	-177	5.55
CAT-I(1)	O-H*...O=C	1.885	254	840	-195	6.12
	C-O*...H-OB	2.114	189	591	-154	4.83
	C-O*...H-N	2.291	119	362	-89	2.79
CAT-I(2)	C-O*...H-N	2.042	212	588	-164	5.15
OH-I(1)	C-O*...H-N	1.997	235	636	-180	5.65
	H-O*... H-C	2.434	106	308	-72	2.27
OH-I(2)	O-H*... O=C	2.066	191	528	-145	4.55
	O-H*... O=C	2.205	105	419	-108	3.39
	H-O*... H-C	2.419	116	326	-78	2.45
	H-O*... H-C	2.608	79	259	-48	1.53

**Table 3.** NBO analysis of drug delivery systems. Wiberg bond orders, natural charges, and selected second-order perturbation energies  $E^{(2)}$  (donor→acceptor) for hydrogen bonds of the titled complexes calculated at B3LYP/6-31G (d, p). The \* Symbol represents the NT atom

Complex	Atoms	Wiberg bond order	Natural charge*	Natural charge (IXA)	Donor NBO	Type	Acceptor NBO	Type	$E^2$ (kcal mol <sup>-1</sup> )
NT-I	C=C*...H-N	0.003	-0.045	0.426	C=C*	$\pi$	N-H	$\sigma^*$	0.48
AZO-I(1)	N-H*...O-B	0.012	0.418	-0.920	O	LP(2)	N-H*	$\sigma^*$	2.08
AZO-I(2)	N-H*...O=C	0.036	0.436	-0.636	O	LP(1)	N-H*	$\sigma^*$	5.56
CAT-I(1)	O-H*...O=C	0.059	0.539	-0.677	O	LP(1)	H*	LP*(1)	11.31
	C-O*...H-O-B	0.034	-0.750	0.510	O	LP(1,2)	H	LP*(1)	6.30
	C-O*...H-N	0.021	-0.723	0.451	O*	LP(1)	H	LP*(1)	3.15
CAT-I(2)	C-O*...H-N	0.029	-0.726	0.439	O*	LP(1)	N-H	$\sigma^*$	7.05
OH-I(1)	C-O*...H-N	0.037	-0.780	0.447	O*	LP(2)	N-O	$\sigma^*$	7.86
	H-O*... H-C	0.012	-0.754	0.284	O*	LP(1,2)	C-H	$\sigma^*$	2.71
OH-I(2)	O-H*... O=C	0.040	0.503	-0.670	O	LP(3)	H*	LP*(1)	8.58
	O-H*... O=C	0.028	0.500	-0.670	O	LP(3)	H*	LP*(1)	4.82
	H-O*... H-C	0.018	-0.765	0.278	O*	LP(2)	C-H	$\sigma^*$	2.34
	H-O*... H-C	0.012	-0.774	0.272	O*	LP(2)	C-H	$\sigma^*$	1.23

### NBO analysis

NBO analysis is one of the most essential methods for describing the nature of HBs.<sup>47,48</sup> This method interprets the electronic wave function based on a set of occupied Lewis and unoccupied non-Lewis localized orbitals. The anti-bonds typically play the primary role in delocalization from the idealized Lewis structure. The strength of delocalization interactions, which could be identified from the Fock matrix in the NBO basis, has been estimated by second-order perturbation energy ( $E^{(2)}$ ). The Wiberg bond orders<sup>30</sup> of hydrogen bond bridges between drugs and NTs are reported in Table 3. The variation trend in Wiberg bond orders is consistent with the hydrogen bond lengths listed in the first column of Table 2, in the sense that as the HB length increased, the Wiberg bond orders decreased. The most important natural charges over the atoms of HB bridges and second-order perturbation energies ( $E^{(2)}$ , donor → acceptor)

in the IHB interactions are given in Table 3.

The high positive natural charge on the hydrogen atoms in HB bridges is consistent with the HB strength obtained from the QTAIM results. Additionally, the high value of the second-order perturbation energy (LP (1)  $O_{IXA} \rightarrow LP^* (1) H_{CAT-NT}$ ) in the CAT-I(1) complex confirms our previous results. Considering the charge transfers in this complex, it was revealed that CAT-NT is a proton donor in one of the HBs and a proton acceptor in another HB, which balances the charge transfer in this complex. The NT-I complex's  $E^{(2)}$  minimum value of ( $\pi C=C_{NT} \rightarrow \sigma^* N-H_{IXA}$ ) indicates weak charge transfer from the nanotube to the drug molecule. This result agrees with the QTAIM results and the MO analysis in section 3.5. A complete assessment of charge transfers indicated minor  $E^{(2)}$  values (less than 1.0 kcal/mol) between two units of IXA and *f*-NTs, except for the HB bridges in Table 3. Considering the results of the previous sections about



from the B3LYP to  $\omega$ B97XD level. For example, the calculated  $E_g$  for IXA at  $\omega$ B97XD was approximately 3.94 eV more than that of B3LYP. Although the calculated values are very different at the two levels of theory, the pattern of their changes is almost identical. A comprehensive review of Table 5 shows a significant decrease in the NT energy gap and chemical hardness by nanotube functionalization. Additionally, the lowest energy gap is related to the OH-NT and OH-I complexes, which increase the conductivity of these complexes at a constant temperature.<sup>51</sup>

HOMO-LUMO orbital diagrams of IXA, NT, NT-I, and more stable *f*-I complexes at two levels of theory are shown in the supplementary material (Figures S1 and S2). Both figures indicate that the HOMO and LUMO orbitals in the NT-I structure were placed homogeneously throughout the nanotube. In contrast, at *f*-I complexes, these orbitals accumulated in different sites of the nanotubes. As expected, the distribution of frontier orbitals depends on the nature of substitution and its position on the NT sidewall. In the OH-I(2) profile, the HOMO orbitals were focused around the hydroxyl groups of the NT wall. Therefore, these regions could be more suitable for drug adsorption and electron transfer.

The accumulation of LUMOs near the end OH groups of the OH-I(2) complex shows that the two ends of the nanotube could also be appropriate sites for electrostatic interactions. Because in this research, we have compared the organic-functionalized groups on the sidewall of the nanotube, this configuration has not been considered. The CAT-I(1) and AZO-I(2) profiles (Figure S1 and Figure S2 in the orbitals on one side of the nanotube. Especially in CAT-I(1), the buildup of orbitals increased near the hydrogen atom,

**Table 5.** Energy gap ( $E_g$ ) and chemical hardness ( $\eta$ ) of IXA, NT, *f*-NTs, and more stable complexes (all of in eV) in the gas phase at two levels of theory with 6-31G (d, p) basis set

Complex	B3LYP		$\omega$ B97XD	
	$E_g$	$\eta$	$E_g$	$\eta$
IXA	5.552	2.776	9.491	4.745
NT	1.695	0.848	4.432	2.216
NT-I	1.693	0.846	4.421	2.211
AZO-NT	1.287	0.644	4.028	2.014
AZO-I(2)	1.291	0.645	4.023	2.011
CAT-NT	1.290	0.645	3.824	1.912
CAT-I(1)	1.288	0.644	3.824	1.912
OH-NT	0.738	0.369	3.100	1.550
OH-I(2)	0.728	0.364	3.122	1.561

**Table 6.** Thermodynamic functions for the adsorption process at 298.15 K and 1.0 atm;  $\Delta_{ads}G^\circ$  and  $\Delta_{ads}H^\circ$  in kcal/mol;  $\Delta_{ads}S^\circ$  in cal/mol.K, dipole moment (DM) in Debye in the gas phase, and solvation energy; SE (kcal/mol) in the water solvent ( $\epsilon = 78.3553$ ). Thermodynamic parameters in the solution are in brackets

Complex	B3LYP/6-31G (d, p)			$\omega$ B97XD/6-31G (d, p)			DM	SE
	$\Delta_{ads}G^\circ$	$\Delta_{ads}H^\circ$	$\Delta_{ads}S^\circ$	$\Delta_{ads}G^\circ$	$\Delta_{ads}H^\circ$	$\Delta_{ads}S^\circ$		
NT-I	-	-	-	-3.45	-15.13	-39.16	2.56	-
AZO-I(2)	3.62	-7.50	-37.30	-4.75	-18.00	-44.43	3.65	-
CAT-I(1)	1.23	-12.40	-47.71	-11.11[-4.02]	-26.45[-19.81]	-51.47[-52.96]	3.08	-22.35
OH-I(2)	1.41	-10.80	-40.95	-13.28[-8.01]	-28.03[-22.51]	-49.47[-48.64]	5.16	-48.86

which was added to the end of NT. For detailed molecular orbital analysis of the most stable configuration, DOS diagrams of CAT-NT and OH-NT calculated at B3LYP/6-31G (d, p) before and after drug loading are presented in the supplementary material (Figure S3). This figure shows that there is no significant change in the energy gap of OH-I(2) and CAT-I(1) complexes after drug loading. Therefore, the adsorption of IXA on the surface of *f*-NT did not perturb the electronic properties of the nanotube. This outcome indicates the weak physical adsorption of the drug on the OH-NT and CAT-NT and introduces them as appropriate drug carriers for IXA.

### Thermodynamic functions and solvation energies

Thermodynamic functions of more stable *f*-I complexes are listed in Table 6. Considering the positive value of CP corrected adsorption energy of NT-I complex (0.47 kcal/mol) the frequency calculations have not been performed for this complex. The noteworthy point in Table 6 is the significant difference in the values of thermodynamic parameters between the two calculation levels. The obtained changes in Gibbs free energy of adsorption at 298.15 K and 1 atm ( $\Delta_{ads}G^\circ$ ) at the B3LYP level were positive and in the 1.23-3.62 kcal/mol range for more stable complexes. The calculated parameters of ( $\Delta_{ads}H^\circ$ ) showed an exothermic process in the adsorption of IXA on the *f*-NT surface for more stable configurations. The negative value of entropy change can be due to the formation of a complex from two isolated molecules. Considering the change in Gibbs free energy, the adsorption process has not been spontaneous or favorable by thermodynamic parameters obtained from the B3LYP level, and it can be introduced as the adsorption-desorption process. The obtained thermodynamic parameters at  $\omega$ B97XD showed exergonic ( $\Delta_{ads}G^\circ < 0$ ) and exothermic ( $\Delta_{ads}H^\circ < 0$ ) processes for all understudy complexes.  $\Delta_{ads}G^\circ$  for the AZO-I(2) complex was calculated to be approximately 1.3 kcal/mol more negative than that of the NT-I complex, which was expected from the adsorption energy results in Table 1. The values of  $\Delta_{ads}G^\circ$  were obtained at -11.11 kcal/mol and -13.28 kcal/mol for CAT-I(1) and OH-I(2), respectively. These parameters exhibit the stability of CAT-I(1) and OH-I(2) thermodynamically. In the last section of calculations, to select the best drug delivery system, the CAT-I(1) and optimization process in the solvent and find the solvation energies. Calculated thermodynamic functions in water are



OH-I(2) structures were reoptimized in water ( $\epsilon = 78.3553$ ). Frequency calculations were performed to approve the also presented (in brackets) in Table 6 for two stable complexes.

As seen, in solution,  $\Delta_{ads}G^\circ$  for the CAT-I(1) and OH-I(2) complexes is negative, and the adsorption process is thermodynamically favorable for both complexes. In the solvent, the absolute value of Gibbs free energy change for OH-I(2) formation is approximately 4 kcal/mol more negative than CAT-I(1). Decreasing the absolute value of  $\Delta_{ads}G^\circ$  from the gas phase to the liquid phase is due to the high Gibbs free energy of  $f$ -NTs in the solvent, which decreases the change in the standard Gibbs free energy of adsorption in the aqueous solution (see equation 7). In addition, the solvation energy (SE) of two stable complexes was obtained from equation (8) and is presented in Table 6. Both complexes are soluble in water, but the SE for OH-I(2) is approximately 26.5 kcal/mol more than the SE of CAT-I(1), which is in agreement with the dipole moment (DM) values. Regarding the abovementioned parameters, OH-NT could be selected as the best carrier for the IXA drug.

#### 4. Conclusions

In this study, the adsorption of IXA on the surface of NT and functionalized NT, including AZO, CAT, and OH-NT, was investigated by the DFT method at the B3LYP/6-31G (d, p) level of theory. Based on the BSSE-counterpoise corrected adsorption energies, the following trend was obtained for more stable complexes of  $f$ -NTs: NT-I << AZO-I < OH-I  $\leq$  CAT-I. QTAIM and NBO analyses indicated that the weak IHB interactions mainly govern the loading of IXA on the  $f$ -NTs. Second-order perturbation energies from NBO analysis proved that the most critical charge transfers between IXA and  $f$ -NTs were due to IHB formation. Reoptimizing more stable complexes by long-range corrected hybrid density functionals slightly reformed the stability pattern of more stable complexes such as CAT-I  $\leq$  OH-I. A study of conceptual DFT descriptors revealed the minimum energy gap and chemical hardness in the OH-I complex. The calculation of thermodynamic functions displayed an exothermic adsorption process for all understudied complexes in the gas phase. The results of the thermodynamic parameters were in excellent agreement with the adsorption energies, QTAIM, NBO, and HOMO-LUMO analyses. Considering the thermodynamic functions of CAT-I and OH-I in the water solvent and the solvation energies, we can introduce OH-I as the best drug delivery system for IXA. Finally, it should be noted that the computational results only provide a theoretical pattern, and the biological environment undoubtedly influences the chemical behavior of drugs.

#### Declaration of Interests


There are no conflicts to declare.


#### Author Contributions

Fatemeh Sadat Mazloom Hosseini: Investigation, Writing-

original draft, Methodology, Software, Mansoureh Zahedi-Tabrizi: Supervision, Writing-Review and editing, Validation, Software, Zainab Moosavi-Tekyeh: Methodology, Software, Writing-Review and editing.

#### Author ID

Seyedeh Fatemeh Sadat Mazloom Hosseini<sup>a</sup> : 0009-0001-7921-2756

Mansoureh Zahedi-Tabrizi<sup>a,\*</sup> : 0000-0002-0448-1548

Zainab Moosavi-Tekyeh<sup>b</sup> : 0000-0003-1266-2653

#### Acknowledgements

The authors thank the supercomputing center of Alzahra University for providing the computational resources.

#### References

1. C. D. Collins, *Cancer Imaging*, **2010**, *10*, 20-31.
2. A. Bonnet, P. Moreau, *Expert Opin. Drug. Saf.*, **2017**, *16*, 973-980.
3. N. Gupta, R. Labotka, G. Liu, A. M. Hui, K. Venkatakrishnan, *Invest. New Drugs*, **2016**, *34*, 338-346.
4. R. Misra, S. Acharya, S. K. Sahoo, *Drug Discov. Today*, **2010**, *15*, 842-850.
5. X. Duan, J. Xiao, Q. Yin, Z. Zhang, H. Yu, S. Mao, Y. Li, *ACS Nano*, **2013**, *7*, 5858-5869.
6. X. Y. Ke, VWL. Ng, S. J. Gao, Y. W. Tong, J. L. Hedrick, Y. Y. Yang, *Biomaterials*, **2014**, *35*, 1096-1108.
7. P. S. Lai, P. J. Lou, C. L. Peng, C. L. Pai, W. N. Yen, M. Y. Huang, T. H. Young, M. J. Shieh, *J. Control. Release*, **2007**, *122*, 39-46.
8. G. Jones, S. K. Goswami, H. Kang, H. S. Choi, J. Kim, *Nanomedicine*, **2020**, *15*, 1341-1356.
9. H. T. Ta, C. R. Dass, I. Larson, P. F. Choong, D. E. Dunstan, *Biomaterials*, **2009**, *30*, 3605-3613.
10. U. Hasegawa, M. Moriyama, H. Uyama, A. J. van der Vlies, *Colloid Polym. Sci.*, **2015**, *293*, 1887-1892.
11. Z. Gu, X. Wang, R. Cheng, L. Cheng, Z. Zhong, *Acta Biomater.*, **2018**, *80*, 288-295.
12. S. Rajoria, S. Rani, D. Chaudhari, S. Jain, U. Gupta, *Pharm. Res.*, **2019**, *36*, 160-175.
13. S. Ijima, *Nature*, **1991**, *345*, 56-58.
14. M. I. Khan, I. Nadeem, A. Majid, M. Shakil, *App. Surf. Sci.*, **2021**, *546*, 149129-149137.
15. M. Bottini, S. Bruckner, K. Nika, N. Bottini, S. Bellucci, A. Magrini, A. Bergamaschi, T. Mustelin, *Toxicol. Lett.*, **2006**, *160*, 121-126.
16. A. Elhissi, W. Ahmed, I. U. Hassan, V. Dhanak, A. D'Emanuele, *J. Drug Deliv.*, **2012**, *2012*, 837327-36.
17. L. Wang, R. J. Mu, L. Lin, X. Chen, S. Lin, Q. Ye, J. Pang, *Int. J. Biol. Macromol.*, **2019**, *133*, 693-701.
18. M. S. Hoseininezhad-Namin, P. Pargolghasemi, S. Alimohammadi, A. S. Rad, L. Taqavi, *Physica E: Low-*



- dimens. Syst. Nanostructures*, **2017**, *90*, 204-213.
19. S. Melchor, J. A. Dobado, CoNTub: *J. Chem. Inf. Comp. Sci.*, **2004**, *44*, 1639-1646.
20. A. D. Becke, *J. Chem. Phys.*, **1993**, *98*, 5648-5652.
21. C. Lee, W. Yang, R. G. Parr, *Phys. Rev. B*, **1998**, *37*, 785-789.
22. M. J. Frisch, G. W. Trucks, H. B. Schlegel, G. E. Scuseria, M. A. Robb, J. R. Cheeseman, G. Scalmani, V. Barone, B. Mennucci, G. A. Petersson, H. Nakatsuji, M. Caricato, X. Li, H. P. Hratchian, A. F. Izmaylov, J. Bloino, G. Zheng, J. L. Sonnenberg, M. Hada, M. Ehara, K. Toyota, R. Fukuda, J. Hasegawa, M. Ishida, T. Nakajima, Y. Honda, O. Kitao, H. Nakai, T. Vreven, J. A. Montgomery, Jr., J. E. Peralta, F. Ogliaro, M. Bearpark, J. J. Heyd, E. Brothers, K. N. Kudin, V. N. Staroverov, R. Kobayashi, J. Normand, K. Raghavachari, A. Rendell, J. C. Burant, S. S. Iyengar, J. Tomasi, M. Cossi, N. Rega, J. M. Millam, M. Klene, J. E. Knox, J. B. Cross, V. Bakken, C. Adamo, J. Jaramillo, R. Gomperts, R. E. Stratmann, O. Yazyev, A. J. Austin, R. Cammi, C. Pomelli, J. W. Ochterski, R. L. Martin, K. Morokuma, V. G. Zakrzewski, G. A. Voth, P. Salvador, J. J. Dannenberg, S. Dapprich, A. D. Daniels, O. Farkas, J. B. Foresman, J. V. Ortiz, J. Cioslowski, and D. J. Fox, Gaussian 09, Revision A.01, Gaussian Inc., Wallingford CT, **2009**.
23. J. Chai, M. Head Gordon, *J. Chem. Phys.*, **2008**, *128*, 084106-15.
24. S. Karimzadeh, B. Safaei, T. -C. Jen, *J. Mol. Liq.*, **2021**, *322*, 114890-114911.
25. S. F. Boys, *F. Mol. Phys.*, **1970**, *19*, 553-566.
26. R. F. W. Bader, A Bond Path: *J. Phys. Chem. A*, **1998**, *102*, 7314-7323.
27. F. B. König, J. Schönbohm, D. Bayles, *J. Comput. Chem.*, **2001**, *22*, 545-559.
28. E. D. Glendening, A. E. Reed, J. E. Carpenter, F. Weinhold. NBO version 3.1. Pittsburgh, PA: Gaussian. Inc. **1992**.
29. E. D. Glendening, C. R. Landis, F. Weinhold, Natural bond orbital methods, *Wiley Interdiscip. Rev. Comput. Mol. Sci.*, **2012**, *2*, 1-42.
30. F. Weinhold, C. R. Landis, Valency and bonding: a natural bond orbital donor-acceptor perspective, Cambridge University Press, **2005**.
31. A. E. Reed, R. B. Weinstock, F. Weinhold, *J. Chem. Phys.* **1985**, *83*, 735-746.
32. R. G. Parr, L. V. Szentpaly, S. Liu, *J. Am. Chem. Soc.*, **1999**, *121*, 1922-1924.
33. R. G. Parr, R. G. Pearson, *J. Am. Chem. Soc.*, **1983**, *105*, 7512-7516.
34. Gauss View 4.1.2, Gaussian Inc., Pittsburg, PA, **2006**.
35. N. M. O'Boyle, A. L. Tenderholt, K. M. Langner, *J. Comput. Chem.*, **2008**, *29*, 839-845.
36. S. Miertuš, E. Scrocco, J. Tomasi, *Chem. Phys.*, **1981**, *55*, 117-129.
37. C. R. Martinez, B. L. Iverson, *Chem. Sci.*, **2012**, *3*, 2191-2201.
38. R. F. Bader, *Acc. Chem. Res.*, **1985**, *18*, 9-15.
39. E. Zarié-Moghaddam, M. Zahedi-Tabrizi *Monatsh Chem. Chem. Mon.*, **2019**, *150*, 1267-1274.
40. B. A. Omidvar, S. F. Tayyari, M. Vakili, A. R. Nekoei, *Spectrochim. Acta A Mol. Biomol. Spectrosc.*, **2018**, *191*, 558-565.
41. R. Heidarian, M. Zahedi-Tabrizi, *Curr. Comput-Aided Drug Des.*, **2021**, *17*, 480-491.
42. S. Haghgoo, A.R. Nekoei, *RSC Adv.*, **2021**, *11*, 17377-17390.
43. M. Yahyavi, F. Badalkhani-Khamesh, N. L. *Chem. Phys. Lett.*, **2020**, *750*, 137492-137501.
44. E. Espinosa, E. Molins, C. Lecomte, *Chem. Phys. Lett.*, **1998**, *285*, 170-173.
45. I. Rozas, I. Alkorta, J. Elguero, *J. Am. Chem. Soc.*, **2000**, *122*, 11154-11161.
46. C. F. Matta, R. J. Boyd, An introduction to the quantum theory of atoms in molecules, Wiley-VCH, **2007**.
47. M. Bazrafshan, M. Vakili, S. F. Tayyari, F. S. Kamounah, P. E. Hansen, M. R. Housaindokht, *J. Mol. Struc.*, **2023**, *1272*, 134178.
48. S. Seyedkatouli, M. Vakili, S. F. Tayyari, P. E. Hansen, F. S. Kamounah, *J. Mol. Struc.*, **2019**, *1184*, 233-245.
49. L. R. Domingo, M. Ríos-Gutiérrez, P. Pérez, *Molecules*, **2016**, *21*, 748-770.
50. S. Emamian, M. Soleymani, S. S. Moosavi, *New J. Chem.*, **2019**, *43*, 4765-4776.
51. C. Kittel, Introduction to Solid State Physic, Wiley, **2004**.